ADVANCED HEALTHCARE MATERIALS
www.advhealthmat.de

Injectable, Antibacterial, and Hemostatic Tissue Sealant Hydrogels

Reihaneh Haghniaz, Hossein Montazerian, Atiya Rabbani, Avijit Baidya, Brent Usui, Yangzhi Zhu, Maryam Tavafoghi, Fazli Wahid, Han-Jun Kim, Amir Sheikhi,* and Ali Khademhosseini**

Hemorrhage and bacterial infections are major hurdles in the management of life-threatening surgical wounds. Most bioadhesives for wound closure lack sufficient hemostatic and antibacterial properties. Furthermore, they suffer from weak sealing efficacy, particularly for stretchable organs, such as the lung and bladder. Accordingly, there is an unmet need for mechanically robust hemostatic sealants with simultaneous antibacterial effects. Here, an injectable, photocrosslinkable, and stretchable hydrogel sealant based on gelatin methacryloyl (GelMA), supplemented with antibacterial zinc ferrite (ZF) nanoparticles and hemostatic silicate nanoplatelets (SNs) for rapid blood coagulation is nanoengineered. The hydrogel reduces the in vitro viability of *Staphylococcus aureus* by more than 90%. The addition of SNs (2% w/v) and ZF nanoparticles (1.5 mg mL^{-1}) to GelMA (20% w/v) improves the burst pressure of perforated ex vivo porcine lungs by more than 40%. Such enhancement translated to ≈250% improvement in the tissue sealing capability compared with a commercial hemostatic sealant, Evicel. Furthermore, the hydrogels reduce bleeding by ≈50% in rat bleeding models. The nanoengineered hydrogel may open new translational opportunities for the effective sealing of complex wounds that require mechanical flexibility, infection management, and hemostasis.

1. Introduction

Uncontrolled bleeding (i.e., hemorrhage) and infections in surgical and traumatic wounds are associated with prolonged and inefficient healing, which may lead to mortality and morbidity in severe cases.[1–2] Rapid hemorrhage control by sealing the lesion mitigates wound-associated complications. Conventional wound closure techniques, such as suturing and stapling, cause additional damage to soft tissues. These methods are inefficient for bleeding control, resulting in body fluid leakage and parenchyma necrosis.[3,4] Tissue-adhesive hydrogels are promising alternatives to arrest bleeding efficiently as they promote blood coagulation upon adhesion to the wound site.[5–7] To this end, numerous bioadhesive hydrogels have been explored as potential hemostatic sealants to seal bleeding wounds, reducing surgery time and complications.[8–10]

Naturally derived commercial hemostatic sealants include fibrin,[11] collagen,[12] gelatin,[13] and cellulose-based glues.[14]

R. Haghniaz, H. Montazerian, B. Usui, Y. Zhu, H.-J. Kim, A. Khademhosseini
Terasaki Institute for Biomedical Innovation
11570 W Olympic Blvd, Los Angeles, CA90024, USA
E-mail: hanjun@korea.ac.kr; khademh@terasaki.org

R. Haghniaz, H. Montazerian, A. Rabbani, M. Tavafoghi
Department of Bioengineering
University of California, Los Angeles
410 Westwood Plaza, Los Angeles, CA90095, USA

R. Haghniaz, H. Montazerian, A. Rabbani, M. Tavafoghi
California NanoSystems Institute
University of California, Los Angeles
570 Westwood Plaza, Los Angeles, CA90095, USA

A. Rabbani
Akhtar Saeed Medical College
Bahria Golf City46000, Pakistan

A. Baidya
Department of Chemical and Biomolecular Engineering
University of California, Los Angeles
Los Angeles, CA90095, USA

A. Baidya
Department of Chemistry
Faculty of Engineering and Technology
SRM Institute of Science and Technology
Kattankulathur, Tamil Nadu603203, India

The ORCID identification number(s) for the author(s) of this article can be found under https://doi.org/10.1002/adhm.202301551

DOI: 10.1002/adhm.202301551

Most natural sealants have gained interest for internal use as a result of biodegradability.[8,15] Commercial fibrin glues (e.g., Evicel, Tisseel, and Hemaseel) attract platelets locally to the wound.[16,17] Despite their advantages, fibrin-based sealants lack long-term tissue adhesion and are prone to transmitting blood-borne diseases.[18,19] Collagen is another hemostatic sealant that triggers blood clot formation by attracting coagulation factors and inducing thrombin secretion.[20] Gelatin, a denatured collagen derivative, has been abundantly used as a hemostatic agent because of its biocompatibility and low cost.[21] Gelatin-based hydrogel sealants may control bleeding and provide a suitable environment for wound healing.[22] Floseal is an example of a commercial hemostatic hydrogel sealant made up of bovine gelatin and human thrombin.[23] One of the drawbacks associated with this class of bioadhesives is poor mechanical integrity and weak tissue adhesion.[24] Recently, photocrosslinkable gelatin methacryloyl (GelMA) hydrogels have been used as mechanically robust and bioadhesive platforms.[25–27] In addition, GelMA hydrogels are biocompatible and biodegradable, thus a suitable candidate for internal wound sealing.[28–31] Moreover, GelMA is favorable for cell adhesion as a result of cell-binding motifs, such as arginyl-glycyl-aspartic acid (RGD), which biodegrades in physiological conditions. Accordingly, GelMA facilitates wound healing.[32] Despite these advantages, GelMA does not offer significant hemostatic and antimicrobial properties, which are essential to protect the wound against bleeding and microbial infections.[33]

A simple, cost-effective, and scalable approach to impart hemostatic effects to hydrogels is to incorporate synthetic nanoparticles, such as silicate nanoplatelets (SNs).[34,35] One of the commercial SNs is LAPONITE, which facilitates blood coagulation by platelet attraction.[36] Furthermore, we have previously reported that SN additives improve pre-gel control on double-curved tissue surfaces via increasing viscosity.[36,37] Likewise, nanoparticle additives have been used to impart adhesion[38–39] and antimicrobial properties to hydrogels.[40,34] Excessive use of antibiotics results in antimicrobial resistance, thereby alternative approaches are required.[41,42] Metal nanoparticles, such as silver, have favorable antiseptic properties;[43–46] however, these nanoparticles are costly and induce cytotoxicity depending on surface coating and concentration.[47] Comparatively, zinc-based nanoparticles pose lower toxicity than silver nanoparticles at the same concentration.[48] We have previously synthesized zinc ferrite (ZF) nanoparticles with the chemical formula of $ZnFe_2O_4$, using a co-precipitation method.[49] The ZF nanoparticles (48 ± 3 nm) had antibacterial properties and wound-healing capabilities.

In this study, we will combine visible light crosslinkable GelMA hydrogels with antibacterial ZF nanoparticles and hemostatic SNs to develop injectable, antibacterial GelMA-SN-ZF nanocomposite sealants for wound control. We will examine the synergistic effects of SNs and ZF nanoparticles on the mechanical strength, adhesion, bactericidal, and hemostatic properties of GelMA hydrogels in vitro. Then, the in vivo efficacy of hydrogels will be investigated in rat liver bleeding and artery bleeding models.

2. Results and Discussion

2.1. Synthesis and Chemical Characterization of Hydrogels

The proposed fabrication process of injectable GelMA-SN-ZF hydrogels and their application for sealing open wounds are shown in **Figure 1**a. The pre-polymer solution is prepared via mixing GelMA, ZF nanoparticles, and SNs. In this study, we tailor the ratio of ZF nanoparticles and SNs to optimize the mechanical properties and bioadhesion of GelMA nanocomposite hydrogels. This mixture is then injected in the lesion and cured by shining visible light ($450 < \text{wavelength} < 550$ nm at ≈ 100 mW cm^{-2} light intensity for 4 min) to form a bioadhesive hydrogel. The hydrogel is engineered to promote blood coagulation and to kill bacteria simultaneously at the wound site. The use of visible light for photocrosslinking circumvents biosafety concerns associated with ultraviolet (UV) light and enables deeper light penetration through the hydrogel.[50]

Electrostatically charged moieties enable hemostatic effects in biomaterials.[51] Inorganic disk-shaped SNs (diameter ≈ 30 nm) have negative charges on their faces and positive charges on their edge.[36] As a result of such heterogenous charge distribution, SNs enable dual electrostatic interactions with other charged polymers or nanoparticles.[36] The ζ-potential of GelMA, SNs, ZF nanoparticles, and their mixtures were measured to understand electrostatic interactions between the hydrogel components (Figure 1b). SNs had a negative ζ-potential of −30 mV. Similarly, ZF nanoparticles had a negative ζ-potential of -17 mV, which is attributed to the electronegative species of ferrite components. Mixing these negatively charged nanoparticles with slightly positively charged GelMA decreased the value of ζ-potential, as observed for the GelMA-SN or GelMA-ZF aggregates compared with SNs or ZF nanoparticles, respectively. Note that the values of ζ-potential are rough estimates as the aggregates are irregular and/or non-spherical. Possible intermolecular interactions of hydrogel components are illustrated in Figure 1c. Negative charges of ZF nanoparticles and SNs interact with positively charged amino acid residues on GelMA backbone (such as lysine). Furthermore, SN edges with positive charges electrostatically bind to negatively charged ZF nanoparticles as well as SN surfaces. In addition to electrostatic interactions, both SNs and ZF nanoparticles may form hydrogen bonds with GelMA.

B. Usui
Franklin W. Olin College of Engineering
1000 Olin Way, Needham, MA02492, USA
F. Wahid
Department of Biomedical Sciences
Pak-Austria Fachhochschule
Institute of Applied Sciences and Technology
Haripur22620, Pakistan
H.-J. Kim
College of Pharmacy
Korea University
Sejong30019, Republic of Korea
A. Sheikhi
Department of Chemical Engineering
The Pennsylvania State University
University Park, PA16802, USA
E-mail: sheikhi@psu.edu
A. Sheikhi
Department of Biomedical Engineering
The Pennsylvania State University
University Park, PA16802, USA

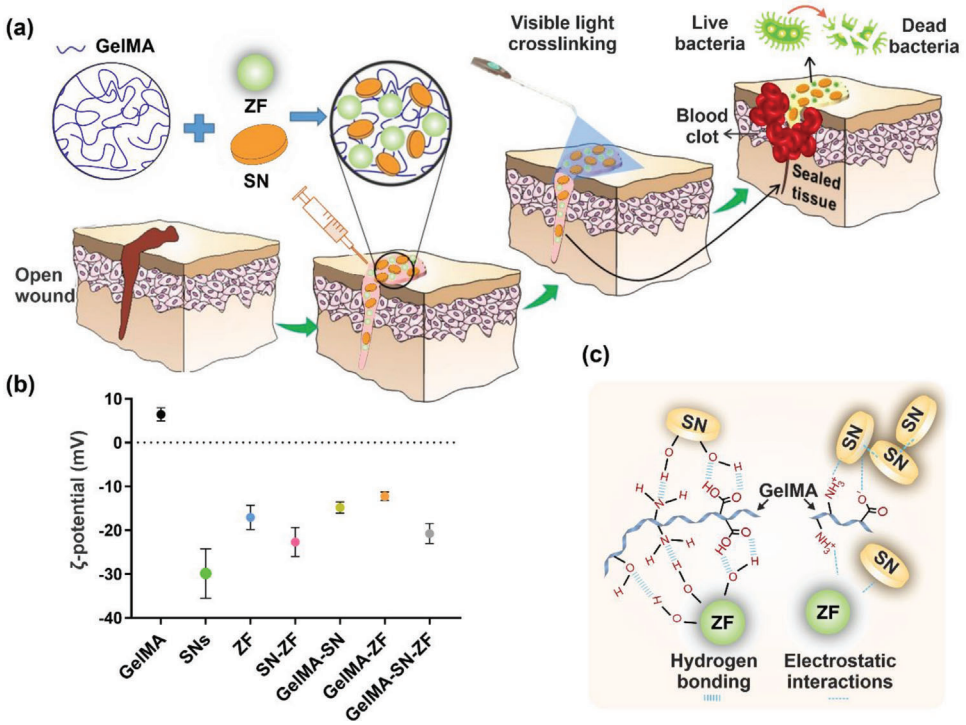

Figure 1. Preparation and application of hemostatic antimicrobial hydrogels. a) Schematic of hydrogel preparation, which involves mixing GelMA (20% w/v) with varying concentrations of SNs and ZF nanoparticles to provide hemostatic and antibacterial properties, respectively. The pre-gel mixture is injected in the lesion, followed by visible light-mediated photocrosslinking to seal and disinfect bleeding wounds. b) ζ-potential of compounds used in the hydrogels, measured at ≈0.1 mg mL^{-1} in Milli-Q water. c) Schematic of interactions among GelMA, SNs, and ZF nanoparticles in the hydrogels.

2.2. Rheological and Mechanical Properties

Rheological characteristics of pre-gel solutions before and during photocrosslinking should be tuned to ensure injectability and timely solidification, respectively. Covalent network formation in hydrogels via photocrosslinking was monitored by the real-time measurement of storage (G') and loss (G'') moduli in response to visible light exposure (**Figure 2**a). G' was significantly increased and surpassed G'' sharply (corresponding to the gel formation point) as photocrosslinking reaction progressed. The results of photocrosslinking time are presented in Figure 2b. The gel formation time for all conditions was <1 min. For further experiments, a photocrosslinking time of 4 min was used to obtain a strong covalent network according to the previous optimizations.[52] The addition of SNs to GelMA hydrogels decreased the gel formation time, whereas the ZF effect was negligible. We attribute the SN effect to the additional internal associations between SNs and GelMA[53] via hydrogen bonding and electrostatic interactions. To further understand this effect, we evaluated the flow of pre-gel solutions under gravity in a vial inversion test,[54] performed at 37 °C. As shown in Figure S1 (Supporting Information), increasing SN concentration increased the viscosity of pre-gel mixtures, possibly as a result of additional noncovalent interactions introduced by SNs. As opposed to GelMA samples containing 30 mg mL^{-1} of SNs, which formed physical gels spontaneously, the hydrogels containing <20 mg mL^{-1} of SNs remained in the sol state and were injectable after 24 h storage at 37 °C. Furthermore, the addition of ZF nanoparticles (1.5 mg mL^{-1}) to GelMA-SN hydrogels, containing 20 mg mL^{-1} of SNs, did not affect the pre-gel flowability and injectability.

Mechanical properties of crosslinked hydrogels were evaluated via oscillatory strain sweep tests, as shown in Figure 2c. The linear viscoelastic (LVE) region was obtained for all GelMA-SN formulations at the shear strain ranging between 0.1% and 10%. This trend was followed by a gradual drop in G', corresponding to the irreversible network rupture or yield point (marked by the arrows). Here, the addition of SNs to GelMA did not significantly affect the yield strain. However, the incorporation of ZF nanoparticles in GelMA-SN composites increased the yield point drastically from ≈10% to over ≈70%. The values of G' in the LVE region at the strain amplitude of 0.1% are presented in Figure 2d. The G' increases by increasing SN concentration due to the SN-mediated noncovalent interactions. The addition of ZF nanoparticles to GelMA-SN hydrogels, however, resulted in an opposite effect and decreased G' by ≈50%, which may be attributed to the partial radical scavenging effect of ZF nanoparticles.[55] Furthermore, cationic edges of SNs bind to anionic ZF nanoparticles, disrupting SN-SN self-assembly. Note that GelMA and GelMA-SN-ZF had statistically nonsignificant G'.

The effect of SNs and ZF nanoparticles on the hydrogel mechanical properties was investigated using the tensile test. Figure 2e shows the test setup schematically. The hydrogels were glued onto a paper holder and mounted on tensile grippers through the paper frames. Then, the sides of the paper frames were cut before starting the tensile test. The tensile stress–strain curves of hydrogels are presented in Figure 2f. The stress

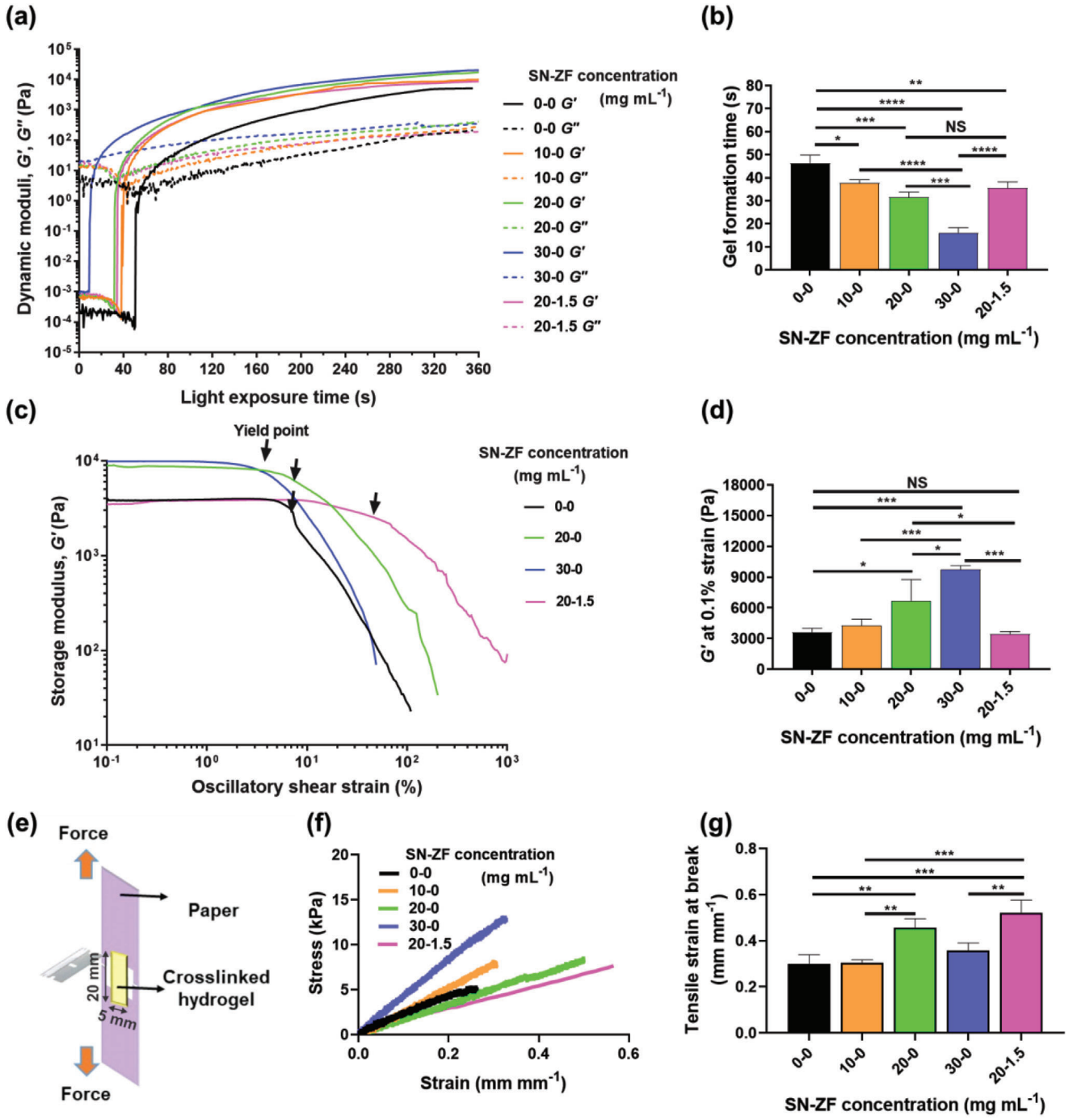

Figure 2. Rheological and mechanical characteristics of hydrogels, containing GelMA (20% w/v) and varying concentrations of SNs and ZF nanoparticles. a) Photocrosslinking kinetics of hydrogels based on storage (G') and loss (G'') moduli, measured under visible light exposure. b) Gel formation time, defined based on the time required for G' to surpass G''. c) Oscillatory strain sweep tests performed on the photocrosslinked hydrogels at a frequency of 1 Hz. Arrows indicate the yield point. d) The values of G' measured from the oscillatory strain sweep test at a strain amplitude of 0.1% and frequency of 1 Hz. e) Schematic of the tensile test setup. f) Tensile stress–strain curves. g) Hydrogels stretchability at varying concentrations of SNs and ZF nanoparticles. Data are presented as the mean of $n = 4 \pm$ standard deviation. Statistically significant differences were stated with p-values less than 0.05 (*$p < 0.05$), 0.01 (**$p < 0.01$), 0.001 (***$p < 0.001$), and 0.0001 (****$p < 0.0001$). NS denotes nonsignificant differences.

increased linearly up to the failure point, which corresponded to the abrupt drop in stress. Although the tensile strength of hydrogels underwent a twofold improvement by adding 20 or 30 mg mL^{-1} of SNs, the addition of ZF nanoparticles decreased the tensile strength to the order of GelMA controls (Figure S2, Supporting Information). This result is consistent with the trends of *G'*, as discussed in Figure 2d. In terms of stretchability, increasing SN content up to 20 mg mL^{-1} increased the elongation at break, whereas a further increase in SN concentration had a detrimental effect on stretchability, potentially due to SN aggregation. The addition of ZF nanoparticles to GelMA-SN hydrogels did not improve hydrogel stretchability. Overall, the enhanced stretchability of GelMA-SN-ZF hydrogels (containing 20 mg mL^{-1} SNs and 1.5 mg mL^{-1} ZF nanoparticles) compared with GelMA hydrogels reduces GelMA brittleness, rendering it suitable for dynamic and expandable organs, such as lung and bladder.

2.3. In Vitro and Ex Vivo Assessments of Sealing

Hydrogel bioadhesion was assessed through burst pressure and wound closure tests. **Figure 3**a shows the burst pressure test setup in which a pierced collagen sheet was sandwiched between two metal parts. The pre-gel mixture was pipetted on the punctured collagen sheet and photocrosslinked to seal the punctured area. The sealing strength was measured by increasing air pressure until the sealant dislodged or ruptured. Figure 3b presents the burst pressure of samples at varying concentrations of SN-ZF compared with a commercial hemostatic hydrogel, Evicel. The addition of SNs or ZF nanoparticles did not significantly affect the burst pressure of GelMA, and the burst pressure measured for hydrogels was at least ≈3 times higher than Evicel.

The wound sealing capacity of hydrogels was studied using the experimental setup shown in Figure 3c. In this setup, porcine skin tissue strips were cut in half and glued back together by the topical application of hydrogels through in situ photocrosslinking. A tensile deformation was then applied until adhesion failed. Figure 3d compares the wound closure strength of hydrogels with that of commercial sealants. The wound closure efficacy of GelMA-SN hydrogels was maximized at the optimal SN concentration of 20 mg mL^{-1}. This trend was in agreement with the results of mechanical properties, as discussed in Figure 2g. Interestingly, introducing ZF nanoparticles to GelMA-SN hydrogels led to a significant improvement (≈23 ± 10% compared with GelMA hydrogels) in wound closure strength, possibly as a result of i) the enhanced compliance of hydrogels with tissue deformations, and ii) ZF-induced noncovalent interactions, including electrostatic and hydrogen bonding with biomacromolecules on tissue surfaces. Notably, all the hydrogels had significantly higher wound closure strengths than Evicel.

Ex vivo burst pressure experiments were conducted using porcine lungs, following a procedure shown in Figure 3e. The pressure at failure was measured and compared with the commercial sealant in Figure 3f. Similar to the wound closure test results, an optimal bioadhesion among GelMA-SN hydrogels was recorded for the samples containing 20 mg mL^{-1} SNs in which the addition of ZF nanoparticles led to further improvements in adhesion strength. The GelMA-SN-ZF hydrogels were able completely seal the fully expanded lungs without any visible air leakage under water. Excessive expansion of lungs resulted in the detachment of GelMA-SN-ZF hydrogels with no observable cohesive failure. The results of ex vivo burst pressure followed a similar trend to wound closure tests (Figure 3d) and ex vivo porcine bladder tissue adhesion tests (Figure S3, Supporting Information), reiterating the synergistic roles of SNs and ZF nanoparticles in bioadhesion enhancement.[56]

2.4. Physical and Structural Properties of Hydrogels

The swelling kinetics of wet hydrogels was assessed in Dulbecco's phosphate-buffered saline (DPBS), as presented in Figure S4a (Supporting Information). All hydrogels reached a maximum swelling ratio of 20%–50% within 4 h. GelMA and GelMA-SN hydrogels at 10 mg mL^{-1} SN content maintained the equilibrium swelling while the other hydrogels underwent deswelling after 4 h. The deswelling of GelMA-SN hydrogels may be attributed to the nanoparticle-induced ion uptake from the buffer.

The average swelling ratio of hydrogels at 4 h is plotted in Figure S4b (Supporting Information). Overall, the swelling ratio increased monotonically with the SN concentration. The addition of ZF nanoparticles to GelMA-SN samples increased the swelling ratio to ≈50%. This effect may be explained by the lower crosslinking density of ZF-incorporated hydrogels, which agrees with their lower *G'*, as discussed above in Figure 2d. We note that excess water uptake causes tissue compression and deteriorates adhesion. The maximum swelling measured here (i.e., ≈50%) is suitable for tissues with a low risk of nerve and blood vessel compression.[57] The degradation profile of hydrogels is presented in Figure S5a (Supporting Information). The degradation rate increased monotonically by increasing SNs. ZF nanoparticles further increased the degradation rate to ≈61% after 21 d of incubation in the collagenase solution (Figure S5b, Supporting Information). We attribute this enhanced degradation to the lower crosslinking density after the incorporation of ZF nanoparticles, as explained above in Figure 2d.

2.5. Antibacterial Effects

The antibacterial efficacy of ZF nanoparticles in GelMA-SN-ZF hydrogels is investigated in **Figure 4**. Figure 4a demonstrates the susceptibility of Gram-positive bacteria, *Staphylococcus aureus* (*S. aureus*) to GelMA-SN-ZF hydrogels after incubation for 12 h on an agar plate. No inhibitory area was formed surrounding GelMA-SN hydrogels (labeled 0), whereas a clear inhibition zone was developed around GelMA-SN-ZF hydrogels. The zone of inhibition expanded by increasing ZF concentration to 1.5 mg mL^{-1}, reaching tetracycline zone of inhibition (positive control, +C). GelMA-SN samples containing ZF nanoparticles (1.5 mg mL^{-1}) inhibited bacterial growth by ≈91% (Figure 4b).

Antibacterial properties were investigated further via a live/dead assay (Figure 4c,d). The amount of green fluorescence (live bacteria) decreased by increasing the ZF content: bacterial viability decreased to <7% by increasing the ZF concentration

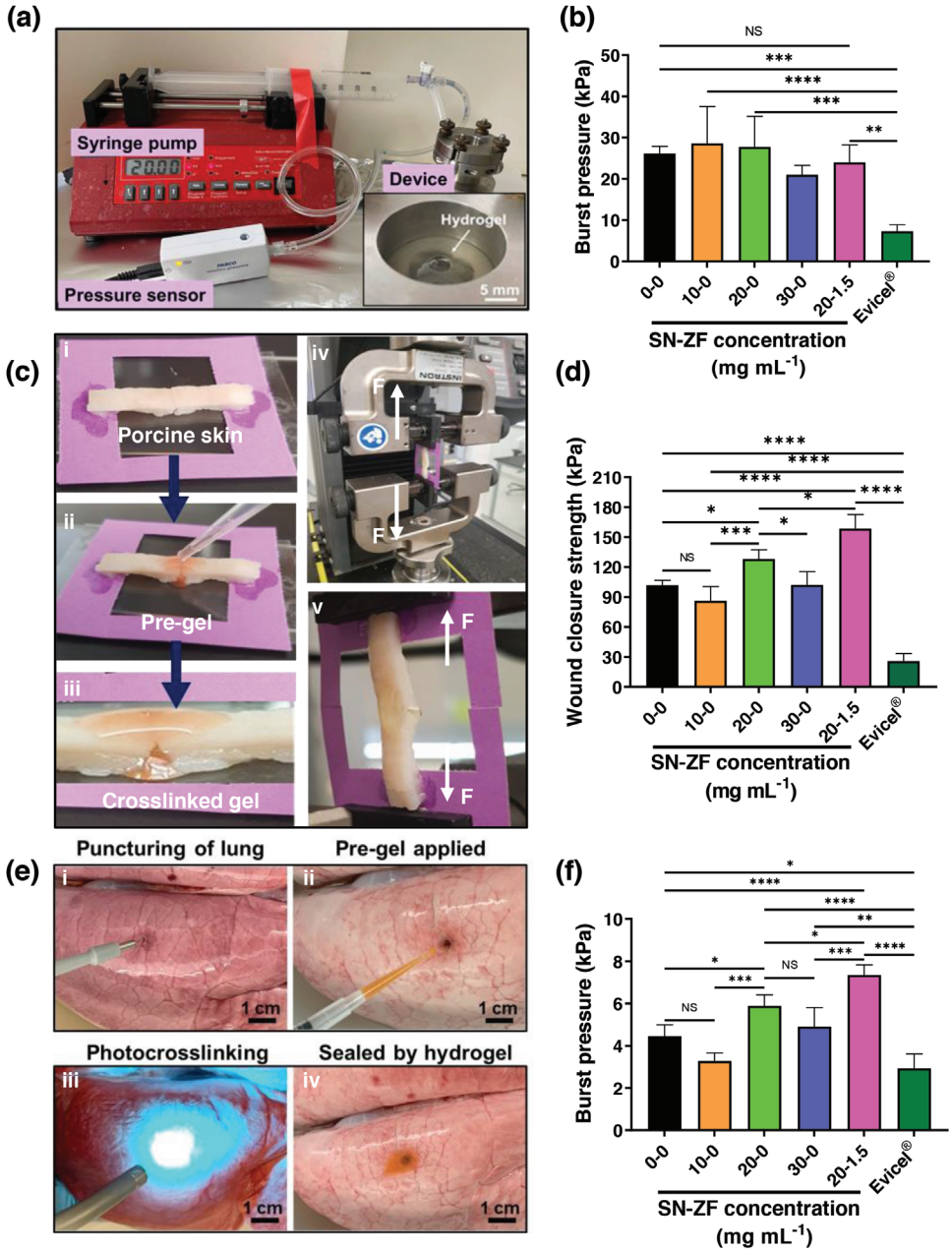

Figure 3. In vitro and ex vivo sealing capability of hydrogels, containing GelMA (20% w/v) and varying concentrations of SNs and ZF nanoparticles. a) Experimental setup and procedures of in vitro burst pressure tests. b) Burst pressure of the hydrogels adhered to wet collagen sheets. c) Wound closure experimental setup, representing i) the formation of an artificial wound in porcine skin, ii) applying a pre-gel mixture to the wound, iii) sealing the wound via visible light photocrosslinking, iv) gripping the specimen between the instrument jaws, and v) measuring the wound closure strength. d) Comparison of the wound closure strength of hydrogels with a commercial hemostat, Evicel. e) Ex vivo burst pressure experiments performed on porcine lung tissues: i) porcine lungs were punctured using a biopsy punch, ii) the pre-gel mixture was applied to the incision, iii) photocrosslinked, and iv) sealed the incision, and the lungs were expanded by injecting air. f) The pressure at the hydrogel failure point was registered as the sealant burst pressure, which was compared with Evicel. Data are plotted as the mean of $n \geq 4$ samples $\pm$ standard deviation. Statistically significant differences were stated with p-values less than 0.05 (*$p < 0.05$), 0.01 (**$p < 0.01$), 0.001 (***$p < 0.001$), and 0.0001 (****$p < 0.0001$). NS denotes nonsignificant differences.

to 1.5 mg mL^{-1}. Therefore, a ZF concentration of 1.5 mg mL^{-1} was used in our formulation. The antibacterial test against Gram-negative bacteria, *Escherichia coli* (*E. coli*) showed ≈52% zone of inhibition and ≈71% reduction in bacterial viability (Figure S6a–d, Supporting Information).

2.6. Hemocompatibility and Hemostatic Properties

Hemocompatibility of hydrogels was characterized by a standard hemolysis assay to evaluate the release of hemoglobin from ruptured red blood cells (RBCs).[58] **Figure 5**a shows the hydrogels

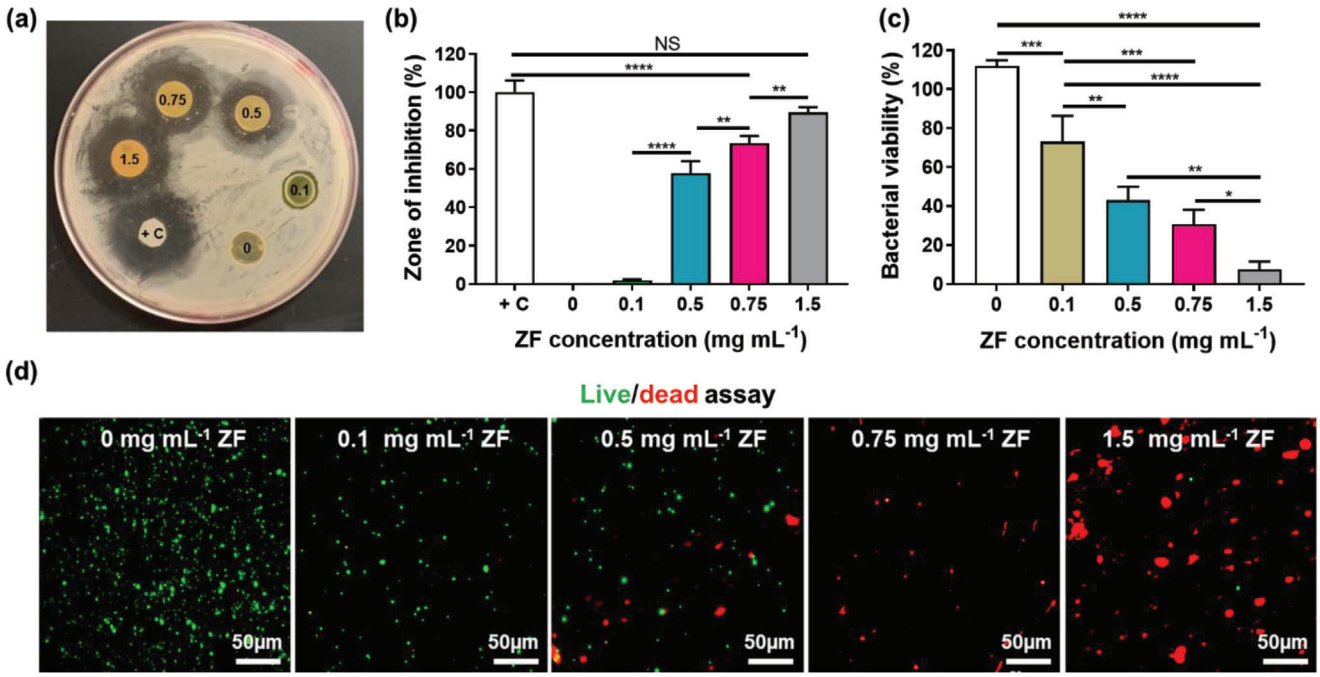

Figure 4. Antibacterial activity of hydrogels against *S. aureus*. a) Photograph representing the zone of inhibition for hydrogels, containing GelMA (20% w/v), SNs (20 mg mL^{-1}), and varying concentrations of ZF nanoparticles (0–1.5 mg mL^{-1}). b) Zone of inhibition for +C (positive control, i.e., tetracycline) compared with hydrogels. c) Bacterial viability, quantified after co-culturing *S. aureus* with GelMA-SN hydrogels, containing varying concentrations of ZF nanoparticles. d) Live/dead fluorescence images of hydrogels co-cultured with *S. aureus* after staining with SYTO 9 (green fluorescence indicating live bacteria) and propidium iodide (red fluorescence indicating dead bacteria). Data represent average ± standard deviation ($n = 3$). Statistically significant differences were stated with *p*-values less than 0.05 (*$p < 0.05$), 0.01 (**$p < 0.01$), 0.001 (***$p < 0.001$), and 0.0001 (****$p < 0.0001$). NS denotes nonsignificant differences.

after exposure to RBCs, followed by centrifugation. The red color of supernatant indicates hemoglobin leakage from damaged RBCs. Unlike the positive controls (PC) with a reddish supernatant, the supernatant for all hydrogels was clear, similar to the negative control (NC), indicating no significant hemolysis. Quantification of hemolysis after the subtraction of background color showed that the incorporation of SNs (20 mg mL^{-1}) and ZF nanoparticles (1.5 mg mL^{-1}) did not affect hemolytic activity significantly (Figure 5b). All conditions resulted in <0.5% hemolysis, which is below the acceptable hemolysis threshold (i.e., 5%).[49,59]

To evaluate the hemostatic properties of hydrogels, a clotting time assay was conducted to monitor clot formation over time (Figure 5c). Blood coagulation was accelerated with increasing SN content, which is attributed to the charge-induced blood coagulation.[36] Likewise, the addition of ZF nanoparticles (1.5 mg mL^{-1}) to the GelMA mixtures led to hemostatic effects. The blood clots after treatment with GelMA-SN-ZF hydrogels were larger and thicker than those formed by pure GelMA hydrogel (Figure 5d). The blood coagulation time was characterized in Figure 5e. No statistically significant difference was found between clotting time in GelMA and controls (nontreated blood). However, the incorporation of SNs in GelMA significantly reduced the clot formation time from 12.3 min (for pure GelMA) to 10.6, 9.3, and 8.3 min for 10-0, 20-0, and 30-0 mg mL^{-1} hydrogels, respectively. Since the clotting time for 20-0 and 30-0 hydrogels were in the same order, we used 20 mg mL^{-1} of SNs in subsequent characterizations.

The hemostatic effect of ZF nanoparticles was evaluated in SN-free GelMA hydrogels. As seen in Figure 5e, the addition of ZF nanoparticles (see sample 0–1.5) reduced clotting time from ≈12 to ≈10 min. The hemostatic effect of ZF nanoparticles may be attributed to the release of Zn^{2+}, which promotes platelet aggregation, triggering blood coagulation.[60] Note that although ZF nanoparticles have a hemostatic effect in GelMA, this effect was negligible in GelMA-SN hydrogels, which may be attributed to i) low ZF nanoparticle concentration compared with SNs, and ii) attraction of Zn^{2+} to negatively charged SNs. GelMA-SN-ZF hydrogels reduced the clotting time most significantly (i.e., 40%), which was on the order of a commercial hemostat, Surgicel. In addition, the hemostatic efficacy of hydrogels was evaluated spectroscopically. UV–visible absorbance of samples was measured at 10 min clotting time to quantify the coagulation process (Figure 5f).[61] Here, the lowest absorbance value was measured for GelMA-SN-ZF hydrogels, followed by GelMA-SN hydrogels at SN concentrations of 30 and 20 mg mL^{-1}, respectively. The absorbance was comparable with Surgicel and far below the untreated blood control, suggesting significant hemostatic effects in GelMA-SN-ZF hydrogels.

We further investigated the blood clot morphology formed on the surface of hydrogels. A thick platelet-rich blood clot layer was formed on the hydrogel surfaces (shown by an arrow in Figure

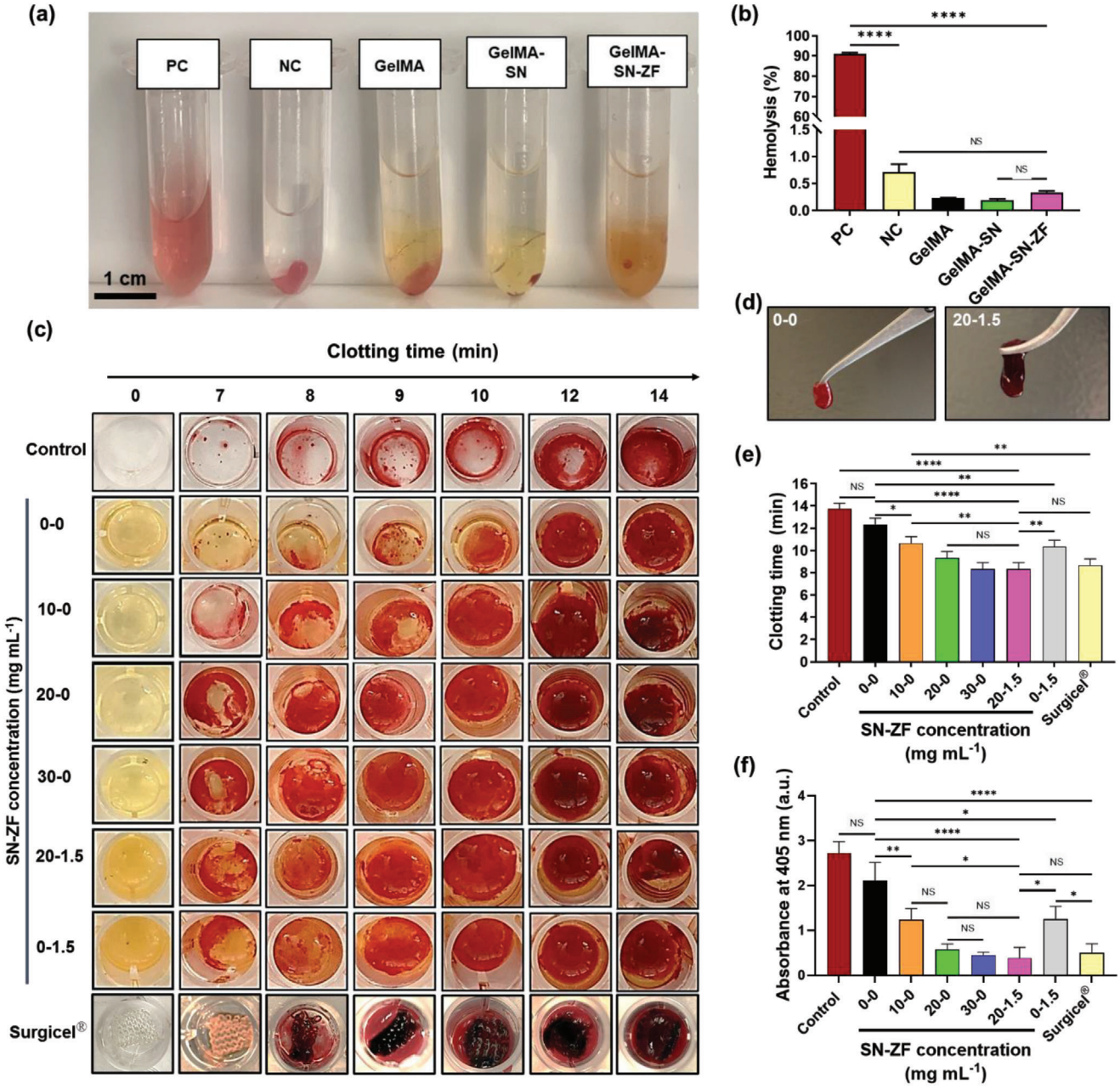

Figure 5. Hemocompatibility and hemostatic properties of hydrogels, containing GelMA (20% w/v) and varying concentrations of SNs and ZF nanoparticles. a) In vitro evaluation of human blood hemolysis upon exposure to hydrogels containing SNs (20 mg mL^{-1}) and ZF nanoparticles (1.5 mg mL^{-1}) for ≈3.5 h. b) Hemolysis ratio, quantified based on the hemoglobin amount released in the supernatant using the cyanmethemoglobin method. NC denotes negative control (i.e., polyethylene glycol, PEG), and PC is the positive control (i.e., Triton X-100). c) Time-dependent clot formation at varying concentrations of SN-ZF compared with untreated blood (control) and the commercial hemostat (Surgicel). d) Images of blood clots formed 10 min after contact with a GelMA hydrogel (20% w/v), and the same GelMA hydrogel containing SN (20 mg mL^{-1}) and ZF (1.5 mg mL^{-1}). e) Clot formation time. f) Absorbance (at 405 nm) of diluted blood supernatant after 10 min exposure to the hemostatic hydrogels. Data are plotted as the mean values of $n \geq 3$ samples ± standard deviation. Statistically significant differences were stated with p-values less than 0.05 (*$p < 0.05$), 0.01 (**$p < 0.01$), 0.001 (***$p < 0.001$), and 0.0001 (****$p < 0.0001$). NS denotes nonsignificant differences.

S7a, Supporting Information). Aggregations of RBCs were observed within the hydrogel pores (Figure S7b, Supporting Information). Furthermore, the activated platelets forming filopodia structures (yellow arrows in Figure S7c, Supporting Information) were observed, which were attached to the fibrin filaments (red arrows in Figure S7c, Supporting Information).

2.7. In Vitro Biocompatibility and In Vivo Systemic Toxicity Evaluation

We have previously demonstrated the biocompatibility of ZF nanoparticles with fibroblast cells,[49] thus here we evaluate the biocompatibility of ZF nanoparticles in combination with SNs

after incorporation in GelMA hydrogels. To evaluate the in vitro biocompatibility of GelMA-SN-ZF hydrogels, NIH/3T3 fibroblast cells grown on the surface of hydrogels were assessed using the live/dead and PrestoBlue assays (see Figure S8, Supporting Information). The results showed that both GelMA-SN and GelMA-SN-ZF hydrogels supported the proliferation and spreading of metabolically active cells. As presented in Figure S8a (Supporting Information), there was no significant difference in green fluorescence (indicating live cells) among GelMA-SN, GelMA-SN-ZF, and GelMA controls over 7 d of culture: all conditions yielded cell viability > 90% (Figure S8b, Supporting Information), suggesting that the integration of SNs and ZF nanoparticles in GelMA had no significant effect on cell viability. In addition, the metabolic activity of cells significantly increased from day 1 to day 7 after cell seeding on the hydrogels without any significant difference among the tested conditions (Figure S8c, Supporting Information).

We assessed the systemic toxicity of the hydrogels in vivo using rat models. During the survival period (four weeks) of experimental groups, no nonspecific toxic reactions such as weight loss, death, or fever - were observed. Figure S9 (Supporting Information) shows the histopathological analyses of main organs (heart, lung, kidney, liver, and spleen) at four weeks after implantation. Microscopic analyses after staining with hematoxylin and eosin (H&E) showed no significant inflammatory or toxic reactions to the degradation products of hydrogels. Thus, the hydrogels are biocompatible and suitable for in vivo applications.

2.8. In Vivo Hemostatic Efficacy of Sealants

We assessed the in vivo sealing performance of engineered GelMA-SN-ZF hydrogels at the optimum composition (i.e., at SN and ZF concentrations of 20 and 1.5 mg mL^{-1}, respectively) using liver and arterial (aortic) bleeding rat models. As shown in **Figure 6**a, a standard liver hemorrhage model was developed by puncturing a median lobe of rat liver with a biopsy punch (4 mm) and applying the pre-gel sealant on the incision, followed by immediate photocrosslinking. To investigate the hemostatic efficacy of hydrogel, the amount of bleeding absorbed by a filter paper was measured immediately after the bleeding stopped. As seen in Figure 6b,c, in the no treatment injury group, the amount of bleeding was significantly higher than other conditions. Treatment of bleeding using GelMA hydrogels did not result in any significant difference from the untreated group. GelMA-SN-ZF hydrogels, however, led to a more efficient wound sealing than GelMA and untreated controls. Hemostatic efficacy of GelMA-SN-ZF hydrogels was on the order of commercial hemostat, Evicel. Both GelMA-SN-ZF hydrogels and Evicel reduced bleeding by more than ≈50%.

We further evaluated the hemostatic efficacy of hydrogels in an arterial (aorta) bleeding model. Figure 6d shows the artery perforation and sealing procedure. In the no-treatment injury group, the perforation of infrarenal aorta resulted in continuous bleeding until the animal was sacrificed, whereas the application of GelMA-SN-ZF hydrogels enabled the sealing of artery and complete prevention of bleeding. The commercial hemostat, Evicel did not stop aorta bleeding and was washed away under blood pressure due to the lack of adhesion. These results suggest that GelMA-SN-ZF hydrogels seal parenchymal bleeding in tissues such as the liver and also withstand blood pressures of abdominal aorta. Future work should investigate the tissue regenerative capability and immunoactivity of hydrogels. In addition, the performance of sealants in larger animals should be studied for clinical translation.

3. Conclusions

Injectable hydrogels are growing rapidly to replace conventional wound closure techniques, such as suturing and stapling. Therefore, biocompatible tissue adhesive hydrogels with hemostatic and antibacterial properties are in high demand, particularly in patients with wound healing disorders. In this study, a naturally derived GelMA-based hydrogel containing SNs and ZF nanoparticles with bioadhesion, hemostatic, and antibacterial properties was developed for sutureless wound closure applications. The hydrogel formulation was engineered to maximize adhesion, hemostasis, and antibacterial efficacy using the lowest possible concentration of nanoparticle additives. The SN additives enabled rapid blood coagulation (up to ≈40% faster coagulation time in vitro and >50% less bleeding in vivo). Furthermore, the hydrogels had significant improvements in bactericidal properties against some Gram-negative and Gram-positive strains. The GelMA-SN-ZF were biocompatible, promoted cell growth in vitro, and did not cause systemic toxicity in rats. Furthermore, the addition of SNs and ZF nanoparticles improved hydrogel tissue adhesion. This work shows that GelMA-SN-ZF hydrogels are a promising candidate for sealing complex wounds.

4. Experimental Section

Materials: Zinc chloride, oleic acid, iron (III) chloride hexahydrate, tetracycline hydrochloride, calcium chloride (0.1 M), sodium hydroxide, porcine skin gelatin type A (300 g bloom strength), *N*-vinylcaprolactam (VC, ≥98% purity), triethanolamine (TEA, ≥99% purity), eosin Y, Triton X-100, polyethylene glycol (PEG, Mn = 400), methacrylic anhydride (MA, >90% purity), pure human hemoglobin, and Drabkin's solution were supplied by Sigma-Aldrich (MO, USA). Different sizes of biopsy punches were procured from Integra Miltex (NJ, USA). LAPONITE XLG-XR with low heavy metal content was bought from BYK Additives & Instruments (MO, USA). Evicel fibrin sealant by Ethicon was obtained from DOTmed (NY, USA). Ultrapure Milli-Q water was purchased from Millipore (MA, USA). Neutral buffered formalin (NBF, 10% v/v) and hematoxylin were purchased from Leica Biosystems, IL, USA. Isoflurane was procured by Piramal (PA, USA). Collagen sheets (collagen sausage casing, 33 mm) were supplied by Weston (NC, USA). *S. aureus*, 25923, *E. coli*, 25922, and murine fibroblast cells (NIH/3T3) were supplied by ATCC (VA, USA). Spectrum dialysis tubing with molecular weight cutoff (MWCO) of 12–14 kDa, Surgicel by Ethicon, Sylgard 184 silicone elastomer kit for fabrication of polydimethylsiloxane (PDMS) mold, carprofen, enrofloxacin, Bacto tryptic soy broth (TSB), tryptic soy agar (TSA), ethanol, paraformaldehyde (PFA, 4% v/v), normal saline (0.9% w/v), PrestoBlue cell viability reagent, and both the cell as well as bacterial LIVE/DEAD viability/cytotoxicity kits were bought from Fisher Scientific (PA, USA). All the supplies for maintaining and passaging the cells, all the cell culture supplies such as media, serum, antibiotic, trypsin-EDTA 0.25%, 1×), and DPBS (1×) were bought from Gibco (NY, USA).

Preparation of ZF Nanoparticles: ZF nanoparticles with the chemical formula of $ZnFe_2O_4$ were prepared following a co-precipitation method as explained previously.[49] Briefly, an aqueous solution of iron (III) chloride ($FeCl_3$) and zinc chloride ($ZnCl_2$) was made at a Zn/Fe molar ratio of

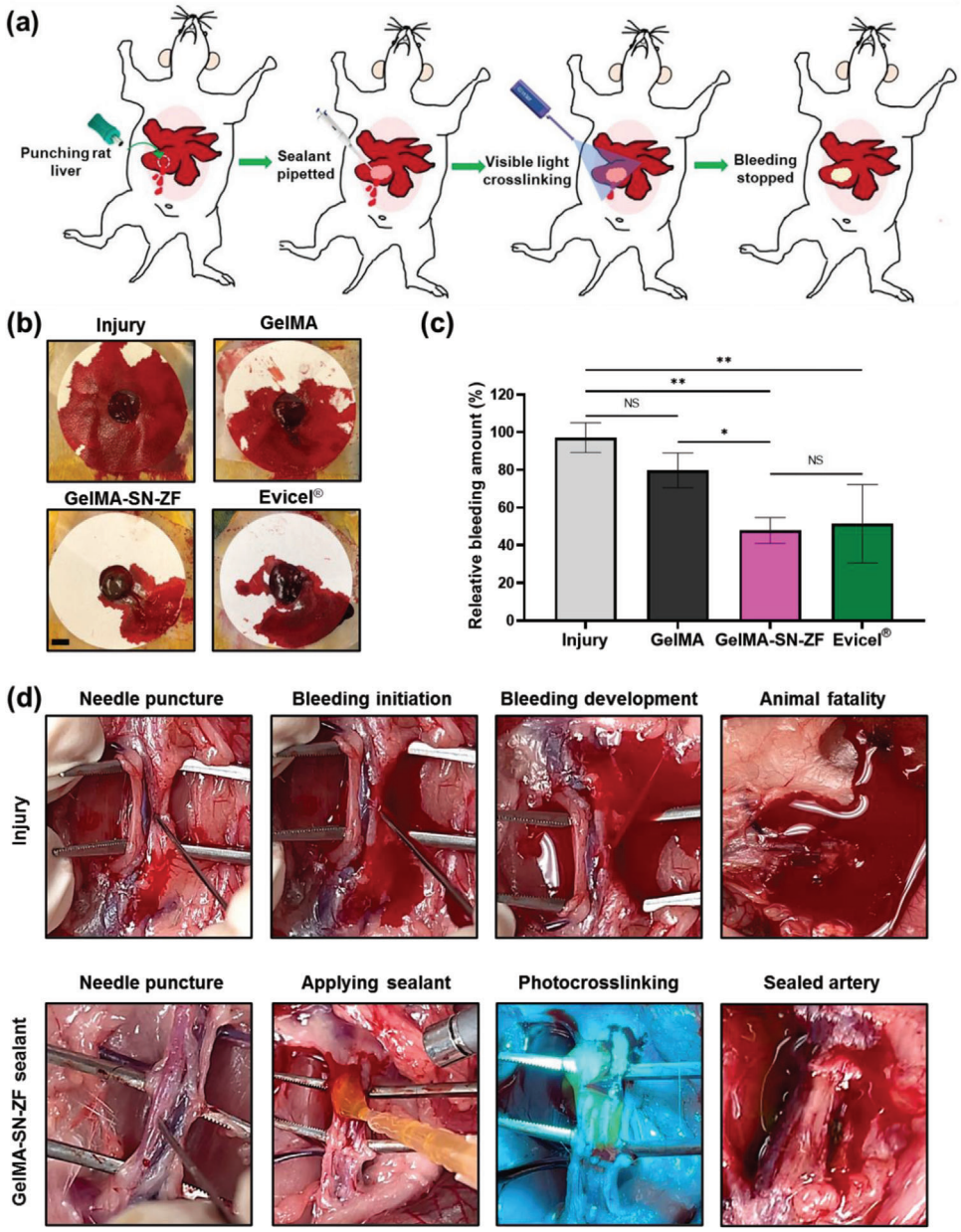

Figure 6. Hemostatic efficacy of hydrogels in rat liver and artery bleeding models. a) Application of engineered GelMA-SN-ZF hydrogels, containing GelMA (20% w/v), SNs (20 mg mL^{-1}), and ZF nanoparticles (1.5 mg mL^{-1}) to prevent hemorrhage in a rat liver hemorrhage model. b) Snapshots of blood uptake by filter papers in different experimental groups. c) The relative amount of bleeding following treatment with GelMA-SN-ZF sealants as compared with the untreated injury group and commercial hemostat, Evicel. d) Sealing arterial bleeding using the GelMA-SN-ZF sealants. In the no treatment injury experiment, the arterial puncture resulted in fatal bleeding, whereas the hydrogel sealants effectively prevented the post-puncture bleeding. Data are shown for $n = 6$ animals per group. Statistically significant differences were stated with p-values less than 0.05 ($*p < 0.05$), 0.01 ($**p < 0.01$), 0.001 ($***p < 0.001$), and 0.0001 ($****p < 0.0001$). NS denotes nonsignificant differences.

1:2. Oleic acid, as a surfactant, was added dropwise to the solution (2–3 droplets in 75 mL of the solution). Thereafter, 3 mol L^{-1} sodium hydroxide as a precipitating agent was incorporated into the metal solution in a dropwise manner under continuous shaking until the desired pH (>12) was attained. The reaction was continued for ≈2 h at 80 °C, followed by centrifugation (6000 rpm, 5 min, at room temperature, Fisher Scientific, PA, USA) to collect the precipitates. The resultant precipitates were rinsed repeatedly with Milli-Q water and ethanol (70% v/v), and heated up to 80 °C to dry, followed by annealing at 500 °C to yield fine powders.[62]

Synthesis of GelMA: GelMA was prepared following protocols explained in our previously published studies.[63,64] Briefly, gelatin from porcine skin (10% w/v) was thoroughly dissolved in DPBS (100 mL) under continuous stirring (240 rpm) at 50 °C. MA (8% v/v) was added to the mixture and stirred in dark for ≈2 h while maintaining the temperature at 50 °C. Equal volumes of DPBS were added to the reactants to halt the reaction. Subsequently, the solution was dialyzed against Milli-Q water for one week using 12–14 kD dialysis tubing, and freeze-dried (Labconco, MO, USA) for 5–7 d until thoroughly dried.

The dried foams were then stored in moist-free condition at room temperature.

Synthesis of Hydrogels: Initially, a stock solution of concentrated GelMA was produced by dissolving the freeze-dried GelMA (40% w/v) in Milli-Q water, containing a double concentration of VC co-monomers (2% w/v), TEA co-initiators (3% w/v), and eosin Y initiators (0.2×10^{-3} M). The mixture was kept at ≈80 °C in dark for ≈15 min until GelMA was dissolved thoroughly. The solution was then maintained at 37 °C until photocrosslinking. To synthesize GelMA-SN mixtures, the stocks of SN dispersion at varying concentrations (0, 20, 40, or 60 mg mL^{-1}) were made in Milli-Q water using a SpeedMixer (3000 rpm, 5 min, FlackTek, Germany), and mixed with an equal volume of the GelMA stock (40% w/v) to yield the mixture with the final SN concentration of 0, 10, 20, or 30 mg mL^{-1} and 20% w/v GelMA. To prepare GelMA-SN-ZF mixture, the concentrations of GelMA and SNs were kept constant at 20% w/v, and 20 mg mL^{-1}, respectively, while the final concentration of ZF nanoparticles varied (0.1, 0.5, 0.75, and 1.5 mg mL^{-1}), followed by the similar mixing procedure explained for the synthesis of GelMA-SN.

To form hydrogels, 200 µL of the pre-gel mixtures were pipetted into disk-shaped PDMS molds (0.8 cm diameter, 0.2 cm height) and covalently crosslinked by visible light irradiation (wavelength of 450–550 nm) for 4 min at an intensity of ≈100 mW cm^{-2} using a Focal Seal Xenon Light Source (LS1000, Genzyme Corporation, Cambridge, MA).

ζ-Potential Measurement: ζ-potentials of GelMA, SNs, ZF nanoparticles, and their mixtures were determined in Milli-Q water using a Malvern panalytical Zetasizer (Nano ZS, WR, UK) supplied with a laser (wavelength = 633 nm). The samples were prepared by vigorous mixing using the speed mixer (3500 rpm, 10 min). All the samples were diluted to the concentration of 0.1 mg mL^{-1} and transferred to the folded capillary cell for measurement. All the measurements were performed in triplicates and 12 counts at room temperature with an equilibration time of 60 s.

Rheological Characterization: An MCR 302 series of Anton Paar's modular compact rheometer (Graz, Austria) attached to a parallel stainless-steel sandblasted plate (PP08/S, diameter = 8 mm) was used to analyze the rheological properties. To characterize sol-gel behavior of the samples, hydrogel precursor mixtures (100 µL) were heated to 37 °C. Visible light was continuously exposed to the samples from underneath using a custom-made fixture. All the measurements were conducted at 1 mm gap size where G' and G'' were assessed as a function of time at the constant strain of 1% and the frequency of 1Hz.

For oscillatory strain sweep tests, hydrogels were soaked in DPBS for ≈8 h to attain equilibrium swelling. The swollen hydrogels were cut into 8 mm diameter disks by a biopsy punch. Oscillatory strains were applied to the samples while G' and G'' were measured at varying oscillatory shear strains over 0.1%–1000%. All measurements were conducted at room temperature with a solvent trap installed on the rheometer to minimize solvent evaporation. The yield point was identified as the intersection of linear fits to data at intervals of 10%–30% and 70%–90% of the oscillatory strain span.

Mechanical Characterization: A mechanical testing equipment (Instron 5943, MA, USA) attached to a 100 N load cell was used to characterize mechanical properties of the hydrogels. The data were recorded using Bluehill software (version 3, USA). Tensile tests were conducted on the crosslinked GelMA-SN and GelMA-SN-ZF hydrogels by pipetting the pre-gel mixes (≈200 µL) onto rectangular PDMS molds (2 cm × 0.5 cm × 0.1 cm), followed by photocrosslinking. The cured hydrogels were soaked in DPBS to reach equilibrium swelling. The stress-strain measurements were performed at a steady displacement rate of 4 mm min^{-1}. The slope of linear stress-strain curves at 10% of strain at break was assigned to elastic modulus. Tensile strength was measured based on the maximal stress at the break point.

In Vitro Burst Pressure Assessment: The hydrogel burst pressure was determined following ASTM F2392-04 procedure with minor modifications.[65] In brief, collagen sheets were cut into disks of ≈3 cm diameter and soaked in DPBS for 1 h. The sheets were punctured at their center using a 3 mm biopsy punch and clamped in a custom-designed burst pressure device. Subsequently, 40 µL of the pre-gel was spread over the punctured area and was photocrosslinked. The device was then attached to a pressure sensor (Pasco Scientific, CA, USA), and air was pumped into the device by a peristaltic pump (BT100-1l, Longer Pump, NJ, USA) at a flow rate of 20 mL min^{-1}. Pressure versus time was continuously recorded by the SPARKvue software (version 3.2.1.3, Pasco Scientific, CA, USA). The maximal pressure at the burst point was used to define the burst pressure.

Ex Vivo Wound Closure Experiment: The adhesion strength of hydrogels to tissues was evaluated using porcine skin following the ASTM F2458-05 standard procedure with slight modifications.[66] Fresh porcine skin (2 mm thickness) was purchased from a local butcher shop and was cut into rectangular-shaped pieces of 4 cm × 0.5 cm. The pre-gel mixtures were injected on top of head-to-head contacted skin cuts, followed by photocrosslinking. Subsequently, a tensile displacement was applied to the specimen at a rate of 4 mm min^{-1}. The stress at which the sealant failed was reported as wound closure strength.

Ex Vivo Burst Pressure Test: The adhesion of hydrogels to tissues was evaluated by a burst pressure test according to the protocols published in our previous studies.[56,67] Freshly excised porcine lungs and bladders were purchased from Sierra for Medical Science (CA, USA). Prior to the test, the tissues were examined for defects and leakage. The tissues were punctured using a biopsy punch (diameter = 3 mm). Pre-gel mixtures (200 µL) were administered on the incision site and were photocrosslinked. Finally, the lungs were filled with air until the sealants failed. The maximum pressure corresponding to the failure point was recorded using a pressure sensor (Pasco Scientific, CA, USA) controlled by SPARKvue software.

A similar process was followed to test the burst pressure of porcine bladder tissues. For this purpose, the bladders were punctured using a 3 mm biopsy punch, pre-gel mixtures (200 µL) were pipetted on the incision and photocrosslinked as described before. Subsequently, water was pumped into the bladder at 20 mL min^{-1}, and pressure was monitored continuously. The pressure at the failure point was recorded as the burst pressure.

Scanning Electron Microscopy: Freeze-dried samples were fixed on scanning electron microscopy (SEM) stubs using conductive carbon tapes. The specimens were rinsed with saline and fixed in PFA (4% in DPBS) for 20 min, followed by dehydration using multiple cycles of ethanol rinsing and freeze-drying. The samples were coated with iridium (44 Å thickness) using a sputter coater (South Bay Technology, USA). Supra 40 VP (Zeiss, Germany) SEM was used to capture images at an accelerating voltage of 12 kV.

In Vitro Swelling and Degradation Tests: Swelling tests were performed to determine the water uptake and stability of hydrogels in physiological conditions. To prepare the hydrogels, 200 µL of the pre-gel mixtures were pipetted into the PDMS molds (1 cm diameter, 0.2 cm height) and were photocrosslinked. The initial weight of hydrogels was recorded (W_i). The samples were transferred to a 12-well plate containing DPBS (3 mL) and stored at 37 °C. At each time point, the hydrogels were weighed (W_w), and the swelling ratio was determined based on Equation (1)

$$\text{Swelling ratio } (\%) = [(W_w - W_i)/W_i] \times 100 \quad (1)$$

For the degradation tests, the initial weight of freeze-dried samples was recorded (W_d). Then, the samples were transferred to a 12-well plate containing 3 mL of freshly prepared collagenase type II enzyme (2.5 U mL^{-1} in DPBS), followed by incubating at 37 °C. At the different time points, the hydrogels were washed with distilled water, dried using a freeze-dryer, and weighed (W_t). The enzyme solution was changed twice a week to maintain enzymatic activity. The degradation rate was calculated using the below Equation (2)

$$\text{Degradation rate } (\%) = [(W_d - W_t)/W_d] \times 100 \quad (2)$$

Zone of Inhibition Test: A lyophilized pellet of *E. coli* or *S. aureus* was suspended in 1 mL of TSB and incubated in a shaking incubator (200 rpm, Barnstead MaxQ 4000-7, Cambridge Scientific, MA, USA) overnight at 37 °C. ZF nanoparticles at different concentrations were incorporated in GelMA hydrogels containing 20 mg mL^{-1} SNs. Photocrosslinked hydrogels were sterilized under UV irradiation (wavelength = 250 nm) for at least

1 h prior to the experiment. Subsequently, 100 µL of the bacterial inoculum (≈10^8 CFU mL^{-1}) was evenly spread on a sterile TSA, and hydrogels were placed on TSA. As a positive control, 20 µL of tetracycline solution (500 µg mL^{-1} in Mill-Q water) was pipetted onto a filter paper and exposed to the bacteria on an agar plate. The plates were incubated at 37 °C for 12 h. Further, the clear zone around each sample was measured and normalized by the zone around positive control to calculate the percent (%) zone of inhibition.

Bacterial Viability Assays: Hydrogels were prepared by dispensing the pre-gel mixture (100 µL) to a 96-well plate, by photocrosslinking. The hydrogels were thoroughly washed with DPBS followed by TSB to remove non-crosslinked moieties and subsequently sterilized by UV irradiation for ≈1 h. A single colony of each strain of bacteria was suspended in 1 mL of TSB and optical density at 600 nm ($OD_{600\,nm}$) was adjusted to ≈10^8 CFU mL^{-1} by the addition of TSB. Finally, 100 µL of the bacteria suspension was added to the hydrogel surfaces in each well. Empty wells served as controls. The plates were incubated at 37 °C overnight. Then, $OD_{600\,nm}$ of bacteria suspension on each hydrogel was measured. Bacterial viability was measured via Equation (3)

$$\text{Bacterial viability}\,(\%) = (OD_{600\,nm}\text{of A} - OD_{600\,nm}\text{ of B}) \times 100/\,(OD_{600\,nm}\text{ of C} - OD_{600\,nm}\text{of D}) \quad (3)$$

where A is hydrogel + TSB + Bacteria, B is hydrogel + TSB without bacteria, C is TSB + Bacteria without hydrogel, and D is TSB without bacteria.

Bacterial live/dead assay was performed following the procedure below. The hydrogels photocrosslinked in a 96-well plate were washed with DPBS and TSB. The bacteria of each strain (150 µL, ≈10^8 CFU mL^{-1}) were added to wells and incubated in a shaking incubator (200 rpm) for ≈8 h at 37 °C. The supernatant of each well was transferred to a separate Eppendorf tube and centrifuged at 12 000 rpm for 1 min. The pellets were rinsed with DPBS and resuspended in 500 µL DPBS. SYTO 9 (green fluorescence) and propidium iodide (red fluorescence) were added to the bacteria suspension at concentrations of 3 and 15 × 10^{-6} M, respectively, and incubated in dark for 15 min at 37 °C. A small volume of the mixture (≈5 µL) was added to a glass slide, shielded by a cover glass, and imaged by a fluorescence microscope (Axio Observer 5, Zeiss, Germany) excitation/emission of 490/520 nm for SYTO 9 and excitation/emission of 490/635 nm for propidium iodide.

Hemocompatibility Assay: To evaluate hemocompatibility of the hydrogels, a hemolysis assay was performed according to the standard protocol, ASTM E2524-08.[68] Heparinized whole blood from healthy human donors was supplied by Zenbio (NC, USA). Prior to the assay, a standard curve was obtained using varying concentrations of pure human hemoglobin (0.025–18 mg L^{-1}). Blood (20 µL) was mixed with Drabkin's reagent (5 mL) and absorbance was read at 540 nm using a UV–vis spectrometer, Synergy microplate reader (BioTek, VT, USA), to measure hemoglobin content in the blood. The concentration of the hemoglobin was then adjusted to 10 ± 2 mg L^{-1} by diluting the blood with DPBS. Subsequently, hydrogels were prepared as explained earlier and placed in Eppendorf tubes containing 900 µL of diluted blood (ratio 1:8 in DPBS). PEG (4.4% v/v in DPBS) and triton X-100 (1% v/v in DPBS) were also added to the diluted blood as negative and positive controls, respectively. The samples were then incubated in water bath shaker (Fisher Scientific) for 3 h ± 15 min at 37 °C. Subsequently, the samples were centrifuged at 14 000 rpm for 15 min. 100 µL of the supernatant was added to a 96-well plate containing an equivalent amount of Drabkin's reagent. The plate was shaken (100 rpm, room temperature) for ≈15 min in dark. Then, the absorbance at 540 nm was measured against the blank reagent. The concentration of cell-free hemoglobin in each sample was calculated based on the standard curve. Ultimately, hemolysis (%) was measured using Equation (4)

$$\text{Hemolysis}\,(\%) = 100 \times \text{sample's hemoglobin concentration} / \text{total blood hemoglobin}\,(\sim 10\text{ mg L}^{-1}) \quad (4)$$

In Vitro Blood Clotting Test: Whole human blood with sodium citrate (≈3.8% w/v) anticoagulant was purchased from Zenbio (NC, USA) and used in the experiments following an approved protocol by the Institutional Review Board. The collected blood was used in the experiment within 24 h of withdrawal.

For the clotting test, the pre-gel mixture (200 µL) was photocrosslinked in a 48 well-plate. To start clotting, calcium chloride (0.1 M) was mixed with the blood at a ratio of 1:9 and shaken for ≈10 s. The blood was then pipetted (200 µL) onto each hydrogel sample or into the empty wells as a control. At each time point, the wells were gently washed with saline repeatedly, until soluble blood thoroughly washed away and only the clots were left behind. The time point at which a uniform clot was formed in the wells was registered as a clotting time.

To compare the extent of clot formation by different types of hydrogels, 10 mL of Milli-Q water was added to the clot at 10 min of clotting time and the solution was centrifuged (100 g, 30 s). Eventually, the absorbance of the supernatant at 405 nm was measured using a microplate reader. The lower value of absorbance was correlated with the greater extent of clot formation.

Biocompatibility Assay: The biocompatibility of hydrogels was determined by culturing NIH/3T3 murine fibroblast cells on the surface of the UV-sterilized crosslinked hydrogels in a 24-well plate. For this purpose, the cells (with confluency of ≥90%) were trypsinized with 0.25% trypsin-EDTA and counted using an automated cell counter (Countless 3, Thermo Fisher Scientific, USA). The cell suspension was prepared in DMEM, supplemented with fetal bovine serum (10% v/v) and penicillin-streptomycin (1% v/v of 10 000 U mL^{-1}), and seeded on the surface of the hydrogels at a cell density of 5000 per well, followed by incubation at 37 °C in a humidified (≈95% humidity) CO_2 (5%) incubator (Forma incubators, ThermoFisher Scientific, USA). To evaluate cells' metabolic activity and proliferation, PresoBlue cell viability assay was conducted after 1, 3, and 7 d of culture. The medium was aspirated from the wells, 100 µL of PresoBlue reagent in 900 µL of the complete medium was added to each well and incubated for ≈1.5 h in dark at 37 °C. Subsequently, the supernatant (100 µL) from each well was transferred to a 96-well plate and the fluorescence was read at the excitation of 530 nm and emission of 590 nm by the plate reader. The hydrogels were thoroughly washed with DPBS and the cells attached to the surface of the hydrogels were stained with LIVE/DEAD viability/cytotoxicity kit on day 7 of culture. The live/dead staining solution was prepared by the mixture of ethidium homodimer-1 (red fluorescence dye, 20 µL) and calcein-AM (green fluorescence dye, 5 µL) in 10 mL of DPBS. This reagent (500 µL) was added to each well and incubated at dark for 15 min in the incubator. Fluorescence images were obtained and were used to quantify cell viability (i.e., the number of live cells divided by total cells) using ImageJ software.

In Vivo Systemic Toxicity Evaluation: All animal trials were approved by the Lundquist Institute (#22590/91-02) Animal Care and Use Committee. The animal experiments were executed aligned with approved guidelines. Sprague-Dawley male rats (seven weeks old, weight range of 250–300 g) were purchased from Charles River Laboratories (CA, USA) and housed at a licensed animal facility. In the biocompatibility assessment study, rats were anesthetized with inhalable anesthesia using isoflurane (1.5% in 100% O_2). The dorsal side (incision line) was shaved and disinfected with iodophor (0.2% w/v) and 70% v/v ethanol. A longitudinal incision of 2 cm was created on the posterior dorsal skin, and two subcutaneous pockets were created on either side of the incision where a hydrogel disc (8 mm diameter, 2 mm thickness) was implanted in each pocket (n = 4 per animal). Implanted hydrogels were UV sterilized for 1 h (254 nm wavelength) before implantation. Post implantation, the incision was closed using surgical staples.

To analyze the systemic toxicological response to the hydrogel, animals were euthanized by CO_2 inhalation at four weeks post-implantation. Vital organs (liver, heart, lung, spleen, and kidney) were immediately harvested and fixed in 10% v/v NBF. Fixed organs were trimmed and processed using standard methods and embedded in paraffin. Paraffin-embedded tissues were cut into 7 µm thick sections and stained with H&E. Histology images were acquired using a Keyence (BZ-X710, IL, USA) inverted microscope.

In Vivo Liver and Artery Bleeding Models: All animal experiments were approved by the Lundquist Institute (#22590/91-02) Animal Care and Use Committee. In vivo bleeding models were conducted on twenty-seven-week-old, male Sprague Dawley rats. Similar to the systemic toxicity evaluation study, under inhalation anesthesia, the ventral side of the hair was clipped and disinfected. For the liver bleeding model, a 1–2 cm incision was made under the ribcage to access the liver. The excess blood at the incision site was absorbed using sterilized gauze. A filter paper was placed surrounding the liver lobe. The liver was then punctured using a biopsy punch (4 mm) and the sterilized pre-gel mixtures (200 µL) were pipetted onto the puncture site, followed photocrosslinking. After that, the bleeding was stopped, and the weight of the blood absorbed to the filter paper was measured.

For the artery (aortic) bleeding model, 27-week-old, male Sprague Dawley rats were used. As described above, all surgical operations were performed under inhalational anesthesia. After median laparotomy, a retractor was placed, and the intestine was gently lateralized to access the infrarenal aorta. Then, the curved forceps were placed under the infra-aorta and caudal vena cava and lifted to block the blood flow from the proximal side. A standardized aortic puncture was set with a 25G needle. Immediately after needle puncture, the pre-gel sealant (100 µL) was applied and photocrosslinked to adhere to the tissue and seal the wound. Finally, after removing the curved forceps, the incisions were checked for bleeding.

Statistical Analyses: All the in vitro tests were conducted in quadruplicates unless noted otherwise. The statistical analyses were carried out using GraphPad Prism version 9.0 (La Jolla, USA). The one-way analysis of variance (ANOVA), followed by Tukey's post-hoc test for multiple comparisons was used in all the experiments except the cytocompatibility PrestoBlue assay, wherein the two-way ANOVA was performed. Statistically significant differences were stated with p-values less than 0.05 ($^{*}p < 0.05$), 0.01 ($^{**}p < 0.01$), 0.001 ($^{***}p < 0.001$), and 0.0001 ($^{****}p < 0.0001$). Nonsignificant differences are noted as NS.

Supporting Information

Supporting Information is available from the Wiley Online Library or from the author.

Acknowledgements

H.-J.K. would like to acknowledge the Basic Science Research Program through the National Research Foundation of Korea (NRF), funded by the Ministry of Education (RS-2023-00240729). A.S. would like to acknowledge the startup fund from The Pennsylvania State University. A.K. would like to acknowledge funding from the National Institutes of Health (1R01EB023052, 1R01HL140618, CA257558, and DK130566). H.M. thanks for the support from Terasaki Institute for Biomedical Innovation.

Conflict of Interest

The authors declare no conflict of interest.

Author Contributions

The original idea was conceptualized, and the experiments were designed by R.H. and A.S. The majority of the experiments were performed and analyzed by R.H. H.M. assisted with mechanical testing and in vitro adhesion tests. The original draft was prepared by R.H. and H.M. A.R. provided ZF nanoparticles and helped R.H. with antibacterial assays and sample preparation. B.U. assisted R.H. with the initial preparation of animals for surgical procedures and editing of the manuscript. Swelling tests were performed by M.T. M.T. also helped R.H. with ex vivo burst pressure test. Analysis of chemical characterization (i.e., ζ-potential) was conducted by A.B. H.-J.K. and R.H. performed animal surgeries and contributed to in vivo data analysis. Y.Z. and F.W. contributed to reading and reviewing the manuscript. The study was conceived of and supervised by H.-J.K., A.S., and A.K. A.S. and A.K. also revised the manuscript. All the authors commented on the manuscript and approved submission.

Data Availability Statement

The data that support the findings of this study are available from the corresponding author upon reasonable request.

Keywords

antimicrobial hemostats, bioadhesives, bleeding wounds, hydrogels, sealants

Received: May 30, 2023
Published online: July 10, 2023

[1] I. Altun, J. Hu, H. Albadawi, Z. Zhang, M. A. Salomao, J. L. Mayer, L. Jamal, R. Oklu, *Adv. Mater.* **2020**, *32*, 2005603.
[2] J. Radwan-Pragłowska, M. Piątkowski, V. Deineka, Ł. Janus, V. Korniienko, E. Husak, V. Holubnycha, I. Liubchak, V. Zhurba, A. Sierakowska, M. Pogorielov, D. Bogdał, *Molecules* **2019**, *24*, 2629.
[3] H. Zhu, X. Mei, Y. He, H. Mao, W. Tang, R. Liu, J. Yang, K. Luo, Z. Gu, L. Zhou, *ACS Appl. Mater. Interfaces* **2020**, *12*, 4241.
[4] S. Baghdasarian, B. Saleh, A. Baidya, H. Kim, M. Ghovvati, E. S. Sani, R. Haghniaz, S. Madhu, M. Kanelli, I. Noshadi, N. Annabi, *Mater. Today Bio* **2022**, *13*, 100199.
[5] H. Montazerian, E. Davoodi, A. H. Najafabadi, R. Haghniaz, A. Baidya, N. Annabi, A. Khademhosseini, P. S. Weiss, *Cell Rep. Phys. Sci.* **2023**, *4*, 101259.
[6] S. Guo, Y. Ren, R. Chang, Y. He, D. Zhang, F. Guan, M. Yao, *ACS Appl. Mater. Interfaces* **2022**, *14*, 34455.
[7] J. H. Wang, C. W. Tsai, N. Y. Tsai, C. Y. Chiang, R. S. Lin, R. F. Pereira, Y. E. Li, *Int. J. Biol. Macromol.* **2021**, *185*, 441.
[8] I. Galanakis, N. Vasdev, N. Soomro, *Rev. Urol.* **2011**, *13*, 131.
[9] C. Sun, X. Zeng, S. Zheng, Y. Wang, Z. Li, H. Zhang, L. Nie, Y. Zhang, Y. Zhao, X. Yang, *Chem. Eng. J.* **2022**, *427*, 130843.
[10] J. Chen, J. He, Y. Yang, L. Qiao, J. Hu, J. Zhang, B. Guo, *Acta Biomater.* **2022**, *146*, 119.
[11] R. Miller, J. C. R. Wormald, R. G. Wade, D. P. Collins, *Br. J. Surg.* **2019**, *106*, 165.
[12] S. Baggio, A. S. Laganà, S. Garzon, M. Scollo, R. Raffaelli, S. Tateo, F. Ghezzi, M. Franchi, *Arch. Gynecol. Obstet.* **2019**, *299*, 1467.
[13] T. Yanagihara, N. Maki, A. I. Wijesinghe, S. Sato, Y. Saeki, S. Kitazawa, M. Yamaoka, N. Kobayashi, S. Kikuchi, Y. Goto, H. Ichimura, S. Watanabe, T. Taguchi, Y. Sato, *Ann. Thorac. Surg.* **2022**, *113*, 1641.
[14] H. S. Yoon, Y. C. Na, K. H. Choi, W. H. Huh, J. M. Kim, *Arch. Craniofac. Surg.* **2019**, *20*, 289.
[15] C. P. Sundaram, A. C. Keenan, *Indian J. Urol.* **2010**, *26*, 374.
[16] R. I. Litvinov, J. W. Weisel, *Matrix Biol.* **2017**, *60*, 110.
[17] W. A. Lam, O. Chaudhuri, A. Crow, K. D. Webster, T. D. Li, A. Kita, J. Huang, D. A. Fletcher, *Nat. Mater.* **2011**, *10*, 61.
[18] L. Ge, S. Chen, *Polymers* **2020**, *12*, 939.
[19] V. Bhagat, M. L. Becker, *Biomacromolecules* **2017**, *18*, 3009.
[20] R. W. Farndale, J. J. Sixma, M. J. Barnes, P. G. de Groot, *J. Thromb. Haemostasis* **2004**, *2*, 561.
[21] M. C. Echave, R. Hernaez-Moya, L. Iturriaga, J. L. Pedraz, R. Lakshminarayanan, A. Dolatshahi-Pirouz, N. Taebnia, G. Orive, *Expert Opin. Biol. Ther.* **2019**, *19*, 773.

[22] M. Wang, C. Wang, M. Chen, Y. Xi, W. Cheng, C. Mao, T. Xu, X. Zhang, C. Lin, W. Gao, Y. Guo, B. Lei, *ACS Nano* **2019**, *13*, 10279.
[23] M. C. Oz, J. F. Rondinone, N. S. Shargill, *J. Cardiovasc. Surg.* **2003**, *18*, 486.
[24] H. Montazerian, E. Davoodi, A. Baidya, M. Badv, R. Haghniaz, A. Dalili, A. S. Milani, M. Hoorfar, N. Annabi, A. Khademhosseini, P. S. Weiss, *Chem. Soc. Rev.* **2022**, *51*, 9127.
[25] K. Yue, X. Li, K. Schrobback, A. Sheikhi, N. Annabi, J. Leijten, W. Zhang, Y. S. Zhang, D. W. Hutmacher, T. J. Klein, A. Khademhosseini, *Biomaterials* **2017**, *139*, 163.
[26] H. Montazerian, A. Baidya, R. Haghniaz, E. Davoodi, S. Ahadian, N. Annabi, A. Khademhosseini, P. S. Weiss, *ACS Appl. Mater. Interfaces* **2021**, *13*, 40290.
[27] Z. Dong, Q. Yuan, K. Huang, W. Xu, G. Liu, Z. Gu, *RSC Adv.* **2019**, *9*, 17737.
[28] Y. Hong, F. Zhou, Y. Hua, X. Zhang, C. Ni, D. Pan, Y. Zhang, D. Jiang, L. Yang, Q. Lin, Y. Zou, D. Yu, D. E. Arnot, X. Zou, L. Zhu, S. Zhang, H. Ouyang, *Nat. Commun.* **2019**, *10*, 2060.
[29] A. Assmann, A. Vegh, M. Ghasemi-Rad, S. Bagherifard, G. Cheng, E. S. Sani, G. U. Ruiz-Esparza, I. Noshadi, A. D. Lassaletta, S. Gangadharan, A. Tamayol, A. Khademhosseini, N. Annabi, *Biomaterials* **2017**, *140*, 115.
[30] Y. Liu, M. B. Chan-Park, *Biomaterials* **2010**, *31*, 1158.
[31] Y. Piao, H. You, T. Xu, H.-P. Bei, I. Z. Piwko, Y. Y. Kwan, X. Zhao, *Eng. Regener.* **2021**, *2*, 47.
[32] K. Yue, G. Trujillo-de Santiago, M. M. Alvarez, A. Tamayol, N. Annabi, A. Khademhosseini, *Biomaterials* **2015**, *73*, 254.
[33] S. Pourshahrestani, E. Zeimaran, N. A. Kadri, N. Mutlu, A. R. Boccaccini, *Adv. Healthcare Mater.* **2020**, *9*, 2000905.
[34] A. K. Gaharwar, N. A. Peppas, A. Khademhosseini, *Biotechnol. Bioeng.* **2014**, *111*, 441.
[35] C. Cha, S. R. Shin, N. Annabi, M. R. Dokmeci, A. Khademhosseini, *ACS Nano* **2013**, *7*, 2891.
[36] A. K. Gaharwar, R. K. Avery, A. Assmann, A. Paul, G. H. McKinley, A. Khademhosseini, B. D. Olsen, *ACS Nano* **2014**, *8*, 9833.
[37] R. Haghniaz, H. J. Kim, H. Montazerian, A. Baidya, M. Tavafoghi, Y. Chen, Y. Zhu, S. Karamikamkar, A. Sheikhi, A. Khademhosseini, *Bioact. Mater.* **2023**, *23*, 314.
[38] S. Rose, A. Prevoteau, P. Elzière, D. Hourdet, A. Marcellan, L. Leibler, *Nature* **2014**, *505*, 382.
[39] Y. Gao, Y. Han, M. Cui, H. L. Tey, L. Wang, C. Xu, *J. Mater. Chem. B* **2017**, *5*, 4535.
[40] M. M. Naik, H. S. B. Naik, G. Nagaraju, M. Vinuth, H. R. Naika, K. Vinu, *Microchem. J.* **2019**, *146*, 1227.
[41] J. M. Blair, M. A. Webber, A. J. Baylay, D. O. Ogbolu, L. J. Piddock, *Nat. Rev. Microbiol.* **2015**, *13*, 42.
[42] M. Frieri, K. Kumar, A. Boutin, *J. Infect. Public Health* **2017**, *10*, 369.
[43] M. Horie, K. Fujita, H. Kato, S. Endoh, K. Nishio, L. K. Komaba, A. Nakamura, A. Miyauchi, S. Kinugasa, Y. Hagihara, E. Niki, Y. Yoshida, H. Iwahashi, *Metallomics* **2012**, *4*, 350.
[44] A. B. Djurišić, Y. H. Leung, A. M. Ng, X. Y. Xu, P. K. Lee, N. Degger, R. S. Wu, *Small* **2015**, *11*, 26.
[45] X. F. Zhang, Z. G. Liu, W. Shen, S. Gurunathan, *Int. J. Mol. Sci.* **2016**, *17*, 1534.
[46] W. R. Li, X. B. Xie, Q. S. Shi, H. Y. Zeng, Y. S. Ou-Yang, Y. B. Chen, *Appl. Microbiol. Biotechnol.* **2010**, *85*, 1115.
[47] A. K. Suresh, D. A. Pelletier, W. Wang, J. L. Morrell-Falvey, B. Gu, M. J. Doktycz, *Langmuir* **2012**, *28*, 2727.
[48] S. Das, R. Aswani, S. J. Midhun, E. K. Radhakrishnan, J. Mathew, *Microb. Pathog.* **2020**, *147*, 104348.
[49] R. Haghniaz, A. Rabbani, F. Vajhadin, T. Khan, R. Kousar, A. R. Khan, H. Montazerian, J. Iqbal, A. Libanori, H. J. Kim, F. Wahid, *J. Nanobiotechnol.* **2021**, *19*, 38.
[50] K. S. Lim, B. J. Klotz, G. C. J. Lindberg, F. P. W. Melchels, G. J. Hooper, J. Malda, D. Gawlitta, T. B. F. Woodfield, *Macromol. Biosci.* **2019**, *19*, 1900098.
[51] H. Montazerian, E. Davoodi, A. Baidya, S. Baghdasarian, E. Sarikhani, C. E. Meyer, R. Haghniaz, M. Badv, N. Annabi, A. Khademhosseini, P. S. Weiss, *Chem. Rev.* **2022**, *122*, 12864.
[52] I. Noshadi, S. Hong, K. E. Sullivan, E. S. Sani, R. Portillo-Lara, A. Tamayol, S. R. Shin, A. E. Gao, W. L. Stoppel, L. D. Black III, A. Khademhosseini, N. Annabi, *Biomater. Sci.* **2017**, *5*, 2093.
[53] N. Rajabi, M. Kharaziha, R. Emadi, A. Zarrabi, H. Mokhtari, S. Salehi, *J. Colloid Interface Sci.* **2020**, *564*, 155.
[54] A. I. Marwan, S. M. Williams, J. R. Bardill, J. Gralla, N. M. Abdul-Aziz, D. Park, *Macromol. Biosci.* **2017**, *17*, 1600473.
[55] C. Vicas, K. Namratha, K. Byrappa, H. Yathirajan, *J. Chem. Pharm. Res.* **2015**, *7*, 1114.
[56] N. Annabi, Y. N. Zhang, A. Assmann, E. S. Sani, G. Cheng, A. D. Lassaletta, A. Vegh, B. Dehghani, G. U. Ruiz-Esparza, X. Wang, S. Gangadharan, A. S. Weiss, A. Khademhosseini, *Sci. Transl. Med.* **2017**, *9*, eaai7466.
[57] C. Ghobril, M. W. Grinstaff, *Chem. Soc. Rev.* **2015**, *44*, 1820.
[58] H. Huang, W. Lai, M. Cui, L. Liang, Y. Lin, Q. Fang, Y. Liu, L. Xie, *Sci. Rep.* **2016**, *6*, 25518.
[59] R. Haghniaz, K. R. Bhayani, R. D. Umrani, K. M. Paknikar, *RSC Adv.* **2013**, *3*, 18489.
[60] G. Marx, J. Krugliak, M. Shaklai, *Am. J. Hematol.* **1991**, *38*, 161.
[61] M. B. Ashour, S. J. Gee, B. D. Hammock, *Anal. Biochem.* **1987**, *166*, 353.
[62] D. D. Andhare, S. A. Jadhav, M. V. Khedkar, S. B. Somvanshi, S. D. More, K. M. Jadhav, *J. Phys.: Conf. Ser.* **2020**, *1644*, 012014.
[63] Z. Li, S. Zhang, Y. Chen, H. Ling, L. Zhao, G. Luo, X. Wang, M. C. Hartel, H. Liu, Y. Xue, R. Haghniaz, K. Lee, W. Sun, H. Kim, J. Lee, Y. Zhao, Y. Zhao, S. Emaminejad, S. Ahadian, N. Ashammakhi, M. R. Dokmeci, Z. Jiang, A. Khademhosseini, *Adv. Funct. Mater.* **2020**, *30*, 2003601.
[64] A. Sheikhi, J. de Rutte, R. Haghniaz, O. Akouissi, A. Sohrabi, D. Di Carlo, A. Khademhosseini, *MethodsX* **2019**, *6*, 1747.
[65] ASTM F2392-04 international, Standard test method for burst strength of surgical sealants, West Conshohocken, PA, **2004**.
[66] ASTM F2458-05 international, Wound closure strength of tissue adhesives, West Conshohocken, PA, **2015**.
[67] M. Tavafoghi, A. Sheikhi, R. Tutar, J. Jahangiry, A. Baidya, R. Haghniaz, A. Khademhosseini, *Adv. Healthcare Mater.* **2020**, *9*, 1901722.
[68] ASTM E2524-08 international, Standard test method for analysis of hemolytic properties of nanoparticles, West Conshohocken, PA, **2013**.